

# Model-based reproduction and validation of the total spectrum of solar flare and their impact on the global environment at the X9.3 event of September 6, 2017

**Kyoko Watanabe** (✉ [kwatana@nda.ac.jp](mailto:kwatana@nda.ac.jp))

National Defense Academy of Japan <https://orcid.org/0000-0003-0321-7881>

**Hidekatsu Jin**

National Institute of Information and Communications Technology (NICT)

**Shohei Nishimoto**

National Defense Academy of Japan

**Shinsuke Imada**

Institute for Space-Earth Environmental Research (ISEE), Nagoya University

**Toshiki Kawai**

Institute for Space-Earth Environmental Research (ISEE), Nagoya University

**Tomoko Kawate**

National Institute for Fusion Science

**Yuichi Otsuka**

Institute for Space-Earth Environmental Research (ISEE), Nagoya University

**Atsuki Shinbori**

Institute for Space-Earth Environmental Research (ISEE), Nagoya University

**Takuya Tsugawa**

National Institute for Information and Communications Technology (NICT)

**Michi Nishioka**

National Institute of Information and Communications Technology (NICT)

---

**Full paper**

**Keywords:** Solar flares, Dellinger effect, Total electron content, Space weather

**Posted Date:** August 6th, 2020

**DOI:** <https://doi.org/10.21203/rs.3.rs-51724/v1>

**License:** © ⓘ This work is licensed under a Creative Commons Attribution 4.0 International License.

[Read Full License](#)

---

**Version of Record:** A version of this preprint was published at Earth, Planets and Space on April 20th, 2021. See the published version at <https://doi.org/10.1186/s40623-021-01376-6>.

# Abstract

We tried to reproduce the total electron content (TEC) variation in the Earth's atmosphere from the temporal variation of the solar flare spectrum of the X9.3 flare on September 6, 2017. The flare spectrum of the Flare Irradiance Spectral Model (FISM) which is most widely used and the flare spectrum from the 1D hydrodynamic model which considers the physics of plasma in the flare loop are used in the GAIA model which is a simulation model of the Earth's whole atmosphere and ionosphere, and calculate the difference of TEC. And then, we compared these results with the observed TEC. When we used the FISM flare spectrum, difference of TEC from the background was in a good agreement with the observation. On the other hand, when the flare spectrum of the 1D-hydro model was used, the result varied depending on the presence or absence of the background. This difference which depends on the models is thought to represent which EUV radiation is primarily responsible for increasing TEC. From the flare spectrum obtained from these models and the calculation result of TEC fluctuation using GAIA, it is considered that the enhancement in EUV emission about 15 to 35 nm is mainly contributes to increasing TEC rather than that of X-ray emission that has been thought to be mainly responsible for sudden ionospheric disturbance (SID). Also, from the altitude/wavelength distribution of the ionization rate of Earth's atmosphere by GAIA, it was found that EUV radiation of about 15–35 nm affects a wide altitude range of 120–300 km, and TEC enhancement is mainly caused by ionization of nitrogen molecules. (265 words)

## 1. Introduction

[2] The radiation from the Sun is the most important ionization and heating energy source for the Earth's upper atmosphere. When the solar flare occurs, the intensity of multi-wavelength electromagnetic emissions suddenly increases. Of these, the increase in X-rays to extreme ultraviolet (EUV) emissions accelerates the ionization and molecular dissociation of atmospheric components in the ionosphere and thermosphere, and it may cause strong increase in electron density. In general, it is thought that ultraviolet (UV) emissions with a long wavelength of 100 nm or more affect the lower atmosphere, while short wavelength EUV and X-rays below 10 nm may also affect the mesosphere. In fact, these short-wavelength UV radiation reaches the ionosphere D region at 60–90 km, causing an increase in electron density in this region. Rapid increase of total electron content (TEC) may degrade accuracy of single frequency GNSS positioning, which is widely used in recent years. In air navigation system, not only positioning accuracy but also safety is important. As the augmentation systems, SBAS (Satellite-based Augmentation System), which covers a wide area by geostationary satellites, and GBAS (Ground-based Augmentation System) have been developed and are in operation. Temporal and spatial variations of TEC can be a threat to these systems (International Civil Aviation Organization, 2010).

[3] The communication failure caused by the absorption of the short-wave by the change of the electron density is known as the Dellinger phenomenon (Dellinger 1937). Generally, the Dellinger phenomenon is considered to be caused by the occurrence of M-class or higher solar flares, and predicted by using the magnitude of the solar flares. However, it has been reported that the Dellinger phenomenon sometimes occurred even in the C-class flare, and that it did not occur even in the X-class flare in observation. From

these results, it is also considered that the flare emissions contributing to the occurrence of the Dellinger phenomenon may also be affected by emissions that is not proportional to the X-ray intensity.

[4] In order to predict not only the Dellinger phenomenon but also the space weather phenomenon caused by the solar flare emissions, it is important to first understand the physical mechanism of the space weather phenomenon. In recent years, the understanding of flare triggers and their physical processes have advanced, and physics-based flare prediction research is rapidly progressing (e.g. Kusano et al., 2020). By applying these physics-based flare prediction methods to the Earth's atmosphere, it will have become possible to predict the effects from solar flare on the Earth's atmosphere.

[5] Therefore, in order to reproduce the observed flare emission, we constructed new flare emission model based on physical processes (Imada et al., 2015; Kawai et al., 2020). In our model, the physical process of the plasma in the flare loop is reproduced by combining the one-dimensional hydrodynamic calculation using CANS (Coordinated Astronomical Numerical Software) 1D package with the CHIANTI atomic database (Dere et al., 2019). Using this model, we reproduced EUV dynamic spectra for some flare events, and compared with observed EUV spectra (Nishimoto et al., 2020b) by the Extreme Ultraviolet Variability (EVE: Woods et al., 2012) onboard the *Solar Dynamics Observatory (SDO)*. We performed our calculation with estimated loop length from observed flare ribbon distance (Nishimoto et al., 2020a). When we compared observed *SDO/EVE* MEGS-A spectra with our calculation results, we found that our result clearly reproduced most of the EUV lines during flare.

[6] In order to examine the effects of the constructed flare irradiance on the Earth's ionosphere, we use an Earth's global whole atmosphere and ionosphere model, GAIA (Ground-to-topside atmosphere and ionosphere model for aeronomy; Jin et al., 2011). The output of solar irradiance spectrum from some models are applied to GAIA as input source of ionospheric photoionization and thermospheric heating, using an ionization cross section model by Solomon and Qian (2005). Vertical total electron content (TEC) is calculated using the results from GAIA runs, and compared with GNSS-TEC observations.

[7] In this paper, we attempted to evaluate the flare emission after flare and its effect on the Earth's atmosphere by a physics-based model study. We focused on the X9.3 flare on September 6, 2017. In Sect. 2, we introduce observational data and the models for flare spectrum and TEC used in this study. Section 3 presents the results of GAIA runs, and Sect. 4 discusses and summarizes the results.

## 2. Observational Data And Models

[8] Two X-class flares occurred on AR102673 on September 6, 2017. Among them, we focused on the X9.3 flare that occurred at 11:53 UT. In this section, we show an overview of the observed solar flare emission spectra by *SDO/EVE* and the model calculation for its reproduction. Then we also show the observation and model calculation of the TEC fluctuation associated with the X9.3 flare.

## 2.1 Solar flares, Dellinger effect, Total electron content, Space weather

[9] The flare emission from the X9.3 flare has been observed in X-rays (0.5–4 Å and 1–8 Å) by the *GOES* (*Geostationary Operational Environmental Satellite*) (Bornmann 1996), and *SDO/EVE* MEGS-B was also observing EUV emission of 360–1060 Å. However, *SDO/EVE* MEGS-A, which was observing 60–370 Å that has a large effect on the Earth's atmosphere, has not been observed due to a failure. Therefore, we estimated flare emission spectrum by the method of Kawai et al. (2020).

[10] In our model, we assumed a semicircular flare loop whose diameter is the distance between two flare ribbons observed in this flare, simulated the plasma motion in the flare loop with 1D-hydro model. Then we obtained the EUV emission strength and its time variation by using CHIANTI. In our model, we calculated only for X9.3 class flare, and the result is shown in Fig. 1 by the blue line during 11:53 – 12:24 UT. Hereafter, this model will be called the “CANS flare model” in this paper.

[11] Here is another prediction model for flare emission named the Flare Irradiance Spectral Model (FISM: Chamberlin et al., 2008). FISM is an empirical model, and provide the spectrum of solar flare in the wavelength range of 1–1900 Å every minute with a wavelength resolution of 10 Å, and the calculation results available on the Web site. Because the time evolution of flare emission is assumed to be proportional to *GOES* soft X-ray in FISM, time evolution of 1–10 Å X-ray in FISM shown in Fig. 1 is almost same as *GOES* X-ray profile of 1–8 Å.

[12] Fig. 2 shows flare spectrum at 12 UT on September 6th, 2017, for each emission model. The red broken line in Fig. 2 is the daily component of FISM, and this spectrum can be use as background. The red line is the FISM flare spectrum, and the green line is the spectrum of the CANS flare model. Since the CANS flare model doesn't consider the continuum component, it can be seen that there is no continuum component around 75–95 nm. The blue line is the sum of the CANS flare model spectrum and the FISM background spectrum.

[13] The flare spectra variation which have the spectra of Fig. 2 and have the light curves of Fig. 1 were input to the GAIA model described later. There are four types of input models, (1) FISM background (“bgd”), (2) FISM flare (“FISM”), (3) CANS flare or background (“CANS/bgd”), and (4) CANS flare and background (“CANS + bgd”).

## 2.2 TEC observation and GAIA

[14] Total electron contents (TEC) in the Earth's ionosphere can be obtained from radio propagation delay between GNSS satellites and receivers (Otsuka et al., 2002; Tsugawa et al., 2018; Shinbori et al., 2020). Figure 3 shows the global distribution of verticalized TEC processed and provided by NICT and Nagoya University. This is the TEC distribution observed at 12 UT on September 6, 2017, when the X9.3 flare occurred. Since the flare occurred around 12 UT, we can see the change of TEC distribution due to the

flare emission by looking at the TEC data around 0°E longitude. In Europe region, sufficient data are obtained around 0°E longitude, so we used 0°E, 25–75°N data for comparative studies.

[15] Fig. 4 shows the time variation of TEC distribution at 0°E and 25–75°N. The upper left of Fig. 4 is the average TEC during the time period from September 1st to 10th, 2017, which can be use as the background. The upper right of Fig. 4 shows the TEC variation observed with the X9.3 flare, and it can be seen that the TEC sharply increases at any latitude around 12UT. As you can see from the background data in the upper left panel in Fig. 4, the amount of TEC increases in the afternoon, but the effect of flare is significantly stronger than the diurnal change, and it is about 1.3 times at the flare peak (Fig. 4 bottom).

[16] Although the actual variation of TEC due to flare emission is obtained in Fig. 4, it is not known from this data as to which wavelength of flare emission causes the TEC variation. Therefore, we used the GAIA model that can calculate ionospheric variation by inputting the flare emission obtained in Chap. 2.1.

[17] GAIA is an Earth's global whole atmosphere and ionosphere model, ionization rates in the upper atmosphere by flare emission depend on the ionization cross sections and the abundance of neutral species there. Figure 5 shows the cross sections of photoionization and photo-dissociative ionization of oxygen atoms, oxygen molecules, and nitrogen molecules, which are the main constituents in the Earth's thermosphere. These cross sections are based on the model of Solomon and Qian (2005). It can be seen that the cross sections for X-rays are smaller than the cross sections for EUV of 15 nm or more by two orders or more. Also, it can be seen that the cross sections for EUV wavelength longer than 60 nm are considerably small depending on the ionization reaction.

[18] Fig. 6 shows the change in ionization rate at each altitude as a result of inputting the flare spectrum of the FISM model (Fig. 2) into GAIA. From this result, it is possible to know which composition is mainly ionized at each altitude in the upper atmosphere. It can be seen that X-rays mainly ionize oxygen and nitrogen atoms at 100–150 km, EUV around 10 nm mainly ionize nitrogen atoms at similar altitude, and EUV around 30 nm mainly ionize a slightly higher layer of nitrogen molecules. EUV about 100 nm also ionizes oxygen molecules around 100 km height.

## 3. Results

### 3.1. TEC obtained from GAIA simulations

[19] As shown in Fig. 7, the four types of solar flare spectra shown in Chap. 2.1 put into GAIA model, and the time variation of TEC were obtained. Run1 inputs FISM background spectrum, which is referred to as background, RUN2, 3 and 4 input "FISM flare", "CANS/bgd", and "CANS + bgd" spectral models, respectively. It can be seen that TEC is significantly increasing in RUN2, 3, and 4 during the X9.3 flare.

[20] Fig. 8 shows the ratio of calculation results of these models compared with Run1. The increase of TEC due to flare emission can be confirmed in all model calculations, and the increase rate is the largest

in Run4 and the smallest in Run3. Since the FISM flare model is input to Run2, the second increase in TEC is observed after 12:30 UT.

## 3.2. Comparison with observed TEC data

[21] The time variation of TEC obtained in Sect. 3.2 was compared with the observed TEC which was shown in Fig. 4. Figure 9 shows the time variation of TEC at 0°E, 44°N. In observed data, there is another large increase of TEC from 12:30 UT after the peak of 12 UT. This is the effect of another flare phenomenon after 12:30 UT, which is seen in the X-ray light curve of Fig. 1. The increase of TEC from 12:30 UT is also seen in RUN2 inputting the FISM model in the GAIA calculation. In the case of CANS flare model input, background emission model is input after 12:30 UT, so the second increase is not seen. In the GAIA model calculation, an increase of TEC is also seen at 15–20 UT, but since this is not seen in the observation, it can be said that this is a characteristic of the GAIA model.

[22] Since the absolute TEC value calculated by GAIA does not match the observed value, we decided to compare the increment from each TEC background. The difference of observed TEC from the background, and the difference of calculated TEC by GAIA from the FISM background was shown in Fig. 10. From Fig. 10, it can be seen that the FISM model result is slightly larger than the observed TEC, but the FISM model well reproduce the observed TEC. The “CANS/bgd” model was 2/3 times of observed TEC, and the “CANS + bgd” model was more than twice the observed TEC.

## 4. Discussion And Summary

[23] We tried to calculate the TEC variations by inputting the temporal variation of the solar flare spectrum for X9.3 flare into the GAIA model, and compared with the observed TEC. In particular, looking at the increments of TEC from background at 0°E, 44°N, FISM model almost reproduced the observed values, the CANS/bgd model showed that 2/3 times, and the “CANS + bgd” model was more than twice the observed value. This discrepancy is considered to represent the intensity ratio of the UV radiation that affects the increment of TEC. By comparing this with the solar flare spectra in Fig. 2, we can guess which wavelength is mainly responsible for the enhancement of TEC.

[24] From Fig. 2, the flare emission with the highest intensity is X-ray, which has an intensity of one order or more compared to EUV radiation. However the fluctuation of TEC is also caused by the combination of emission spectrum, the photoionization cross section (Fig. 5), and the distribution of atmospheric densities. Indeed, as shown in Fig. 6(e), it can be seen that the ionization of the atmosphere mainly at an altitude of 100–150 km is due to X-ray. However, from Fig. 1, the background intensity of X-ray is two orders of magnitude smaller than the flare peak intensity of X-ray, so it is considered that there is no significant difference between the model of “CANS/bgd” and “CANS + bgd”. Figure 2 also shows the background spectrum below 15 nm is smaller than the flare spectrum by one order or more, so we can easily guess that there is no difference of the X-ray intensity between the “CANS/bgd” model and the

“CANS + bgd” model. From this relationship, it can say that X-ray emission is not the main wavelength affecting TEC enhancement.

[25] On the other hand, large spectral difference depending on the type of flare emission model were seen in long wavelength of 75–95 nm. Especially, since the CANS flare model doesn't consider the continuum component, the EUV flux of the “CANS/bgd” model is two orders of magnitude smaller than that of the FISM model. In this wavelength band, the intensity of the “CANS + bgd” model is about 1/3 times from that of the FISM model. However, the TEC in the “CANS + bgd” model at the flare peak at 0°E, 44°N is more than twice that of the FISM model, so the intensity ratio is not consistent with that of UV emissions. From this result, it is considered that the EUV radiation on the long wavelength does not affect the TEC.

[26] The wavelengths which intensity getting stronger in the order of “CANS/bgd”, “FISM”, and “CANS + bgd” are around 15–35 nm emission. Especially around 20 nm, the difference in intensity between the models is about several times, which is almost the same as the difference in the amount of increase in each TEC. The EUV intensity in this wavelength band is one or more orders of magnitude smaller than that of X-rays, but it is about one order of magnitude larger than that of long-wavelength EUV emission, so it is thought that this EUV emission mainly affects the TEC of the Earth's ionosphere. Also, for around 30 nm EUV emission, it has a high ionization rate at a wide altitude of 120–300 km. Ionization is neutralized more quickly at lower altitudes, but 120–300 km is relatively high altitude, so it is believed that ionization will be maintained for some time. Therefore, it is considered that EUV emission with wavelengths around 15–35 nm is the main cause of the increase in TEC.

[27] The FISM's 10 Å wavelength resolution doesn't work, but when reproducing the flare spectrum with our model's 1 Å wavelength resolution, we can identify which EUV line emission is the most dominant line in this wavelength range. The strongest line emission in this wavelength range is the 304Å He II line. In addition, lines such as Fe XII at 195 Å, He II at 256 Å, Fe XV at 284 Å, and Fe XVI at 335 Å are also stronger lines. Of these lines, the Fe lines come from several MK plasmas, and He II is mainly from the chromosphere. From this result, it is considered that the flare emission model can also reproduce TEC difference correctly if it can reproduce flare spectrum of several MK plasmas and emission from the chromosphere.

[28] We discussed the TEC variation due to the X9.3 flare that occurred on September 6, 2017 at this time. Since the analysis of only one case may include the specific feature of only one flare, we will statistically conduct this study in near future to obtain global relationship between flare emission and TEC.

## Abbreviations

CANS  
Coordinated Astronomical Numerical Software  
EUV  
extreme ultraviolet  
EVE

Extreme Ultraviolet Variability  
FISM  
Flare Irradiance Spectral Model  
GAIA  
Ground-to-topside atmosphere and ionosphere model for aeronomy  
GBAS  
Ground-based Augmentation System  
GNSS  
Global Navigation Satellite System  
GOES  
Geostationary Operational Environmental Satellite  
MEGS  
Multiple EUV Grating Spectrograph  
NICT  
National Institute of Information and Communications Technology  
SBAS  
Satellite-based Augmentation System  
SDO  
Solar Dynamics Observatory  
SID  
sudden ionospheric disturbance  
TEC  
total electron content  
UT  
universal time  
UV  
ultraviolet

## **Declarations**

## **Ethics approval and consent to participate**

No applicable

## **Consent for publication**

No applicable

## **Availability of data and materials**

We use the GOES X-ray data provided by NOAA National Centers for Environmental Information <https://www.ngdc.noaa.gov/stp/space-weather/solar-data/solar-features/solar-flares/x-rays/goes/xrs/>. The FISM results are available at <https://lasp.colorado.edu/lisird/> and observational EUV data of SDO/EVE also available at [http://lasp.colorado.edu/eve/data\\_access/eve-flare-catalog/index.html](http://lasp.colorado.edu/eve/data_access/eve-flare-catalog/index.html). The GNSS data collection and processing were performed using the NICT Science Cloud. The Receiver Independent Exchange (RINEX) format data used for GNSS-TEC processing were provided by the following organizations: UNAVCO (<ftp://data-out.unavco.org>), DGRSDUT (<http://gnss1.tudelft.nl>), Arecibo Observatory (<http://www.naic.edu>), CDDIS (<ftp://cddis.gsfc.nasa.gov>), CHAIN (<ftp://chain.physics.unb.ca>), CORS (<ftp://www.ngs.noaa.gov>), GDAF (<ftp://geodaf.mt.asi.it>), BKG (<ftp://igs.bkg.bund.de>), IGS (<ftp://rgpdata.ign.fr>), EUOLG (<ftp://olggps.oeaw.ac.at>), Geoscience Australia (<ftp://ftp.ga.gov.au>), IGSIGN (<ftp://igs.ensg.ign.fr>), KASI (<ftp://nfs.kasi.re.kr>), PNGA (<http://www.geodesy.cwu.edu>), IBGE (<ftp://geofp.ibge.gov.br>), RGCL (<ftp://ftp.itacyl.es>), TNG (<ftp://196.15.132.3>), SOPAC (<ftp://garner.ucsd.edu>), NRC (<ftp://wcda.pgc.nrcan.gc.ca>), GEONET (<ftp://163.42.5.1>), HRAO (<ftp://geoid.hartrao.ac.za>), GRN (<ftp://rinex.smartnetna.com>), GNNZ (<ftp://ftp.geonet.org.nz>), RENAG (<ftp://renag.unice.fr>), SONEI (<ftp://ftp.sonei.org>), FRDN (<ftp://www.crs.inogs.it>), LINZ (<ftp://apps.linz.govt.nz>), ROB (<ftp://gnss.oma.be>), GOP (<ftp://ftp.pecny.cz>), RGE (<ftp://62.99.86.141>), RGNA (<ftp://geodesia.inegi.org.mx>), CENAT (<ftp://ramsac.ign.gob.ar>), INGV (<ftp://bancadati2.gm.ingv.it>), REP (<ftp://158.49.61.10>), SWSBM (<ftp://ftp-out.sws.bom.gov.au>), CORS (<ftp://meristemum.carm.es>), AFREF (<ftp://ftp.afrefdata.org>), WHU (<ftp://igs.gnsswhu.cn>), TLALOCNET (<ftp://tla-locnet.udg.mx>), NCEDC (<ftp://www.ncedc.org>), ODT (<ftp://ftp.odot.state.or.us>), SWEPOS (<ftp://ftp-sweposdata.lm.se>), EUREF (<ftp://www.epncb.oma.be>), IGG (<ftp://ftp.glonass-iac.ru>), SUGAUR (<ftp://eos.ntu.edu.sg>), NMA (<ftp://ftp.statkart.no>), NERC (<ftp://128.243.138.204>), RAMSAC (<ftp://ramsac.ign.gob.ar>), and ERGNSS (<ftp://ftp.geodesia.ign.es>).

## Competing interests

The authors declare that they have no competing interests.

## Funding

This study was supported by the JSPS KAKENHI Grant Numbers JP16H06286, JP16H01187 and JP18H04452.

## Authors' contributions

KW conducted the research and has responsibility for the results presented in this paper. HJ has responsibility for the GAIA calibration and supported this analysis. SN, SI, TK and TK contributed to providing the physics-based flare spectra, and discussion as experts of solar physics. YO, AS, TT and MN contributed to providing TEC data. All authors read and approved the final manuscript.

# Acknowledgements

This study was supported by the JSPS KAKENHI Grant Numbers JP16H06286, JP16H01187 and JP18H04452. Part of this work was performed by the joint research program of the Institute for Space-Earth Environmental Research (ISEE), Nagoya University. The GNSS data collection and processing were performed using the NICT Science Cloud. The Receiver Independent Exchange (RINEX) format data used for GNSS-TEC processing were provided by the following organizations: UNAVCO (<ftp://data-out.unavco.org>), DGRSDUT (<http://gnss1.tudelft.nl>), Arecibo Observatory (<http://www.naic.edu>), CDDIS (<ftp://cddis.gsfc.nasa.gov>), CHAIN (<ftp://chain.physics.unb.ca>), CORS (<ftp://www.ngs.noaa.gov>), GDAF (<ftp://geodaf.mt.asi.it>), BKG (<ftp://igs.bkg.bund.de>), IGS (<ftp://rgpdata.ign.fr>), EUOLG (<ftp://olggps.oeaw.ac.at>), Geoscience Australia (<ftp://ftp.ga.gov.au>), IGSIGN (<ftp://igs.ensg.ign.fr>), KASI (<ftp://nfs.kasi.re.kr>), PNGA (<http://www.geodesy.cwu.edu>), IBGE (<ftp://geofp.ibge.gov.br>), RGCL (<ftp://ftp.itacyl.es>), TNG (<ftp://196.15.132.3>), SOPAC (<ftp://garner.ucsd.edu>), NRC (<ftp://wcda.pgc.nrcan.gc.ca>), GEONET (<ftp://163.42.5.1>), HRAO (<ftp://geoid.hartrao.ac.za>), GRN (<ftp://rinex.smartnetna.com>), GNNZ (<ftp://ftp.geonet.org.nz>), RENAG (<ftp://renag.unice.fr>), SONEL (<ftp://ftp.sonel.org>), FRDN (<ftp://www.crs.inogs.it>), LINZ (<ftp://apps.linz.govt.nz>), ROB (<ftp://gnss.oma.be>), GOP (<ftp://ftp.pecny.cz>), RGE (<ftp://62.99.86.141>), RGNA (<ftp://geodesia.inegi.org.mx>), CENAT (<ftp://ramsac.ign.gob.ar>), INGV (<ftp://bancadati2.gm.ingv.it>), REP (<ftp://158.49.61.10>), SWSBM (<ftp://ftp-out.sws.bom.gov.au>), CORS (<ftp://meristemum.carm.es>), AFREF (<ftp://ftp.afrefdata.org>), WHU (<ftp://igs.gnsswhu.cn>), TLALOCNET (<ftp://tla-locnet.udg.mx>), NCEDC (<ftp://www.ncedc.org>), ODT (<ftp://ftp.odot.state.or.us>), SWEPOS (<ftp://ftp-sweposdata.lm.se>), EUREF (<ftp://www.epncb.oma.be>), IGG (<ftp://ftp.glonass-iac.ru>), SUGAUR (<ftp://eos.ntu.edu.sg>), NMA (<ftp://ftp.statkart.no>), NERC (<ftp://128.243.138.204>), RAMSAC (<ftp://ramsac.ign.gob.ar>), and ERGNSS (<ftp://ftp.geodesia.ign.es>).

## References

1. Bornmann PL, Speich D, Hirman J et al. (1996), GOES X-ray sensor and its use in predicting solar-terrestrial disturbances, *Proceedings of SPIE*, 2812, 291–298
2. Cargill PJ, Bradshaw SJ, Klimchuk JA (2012) Enthalpy-based Thermal Evolution of Loops. III. Comparison of Zero-dimensional Models. *Astrophys J* 758:5
3. Chamberlin PC, Woods TN, Eparvier FG (2006), Flare Irradiance Spectral Model (FISM) use for space weather applications, *Proceedings of the ILWS Workshop*, 153
4. Chamberlin PC, Woods TN, Eparvier FG (2007), Flare Irradiance Spectral Model (FISM): Daily component algorithms and results, *Space Weather*, 5, 7, S07005
5. Chamberlin PC, Woods TN, Eparvier FG (2008) Flare Irradiance Spectral Model (FISM): Flare component algorithms and results. *Space Weather* 6(5):S05001
6. Chamberlin PC, Woods TN, Didkovsky L et al (2018) Solar Ultraviolet Irradiance Observations of the Solar Flares During the Intense September 2017 Storm Period. *Space Weather* 16(10):1470–1487
7. Dellinger JH (1937) Sudden disturbances of the ionosphere. *J Appl Phys* 8(11):732–751

8. Dere KP, Landi E, Mason HE, Monsingnori BC, Young PR (1997) CHIANTI - an atomic database for emission lines. *Astronomy Astrophysics Supplement* 125:149–173
9. Dere KP, Del Zanna G, Young PR, Landi E, Sutherland RS (2019) CHIANTI - An Atomic Database for Emission Lines. XV. Version 9, Improvements for the X-Ray Satellite Lines. *Astrophysical Journal Supplement* 241:22
10. Imada S, Murakami I, Watanabe T (2015) Observation and numerical modeling of chromospheric evaporation during the impulsive phase of a solar flare. *Phys Plasmas* 22:101206
11. International Civil Aviation Organization (2010), *International Standard and Recommended Practices, Annex 10 to the Convention on International Civil Aviation, Volume I, Radio Navigation Aids*
12. Jin H, Miyoshi Y, Fujiwara H et al (2011) Vertical connection from the tropospheric activities to the ionospheric longitudinal structure simulated by a new Earth's whole atmosphere-ionosphere coupled model. *J Geophys Res* 116:A01316
13. Kawai T, Imada S, Nishimoto S, Watanabe K, Kawate T (2020) Nowcast of an EUV dynamic spectrum during solar flares. *J Atmos Solar Terr Phys* 205:105302
14. Klimchuk JA, Patsourakos S, Cargill PJ (2008) Highly Efficient Modeling of Dynamic Coronal Loops. *Astrophys J* 682:1351–1362
15. Kusano K, Iju Y, Bamba S, Inoue (2020) A physics-based method that can predict imminent large solar flares. *Science* 369:6503, 587–591
16. Nishimoto S, Watanabe K, Imada S et al. (2020a), Statistical and observational research on solar flare EUV spectra and geometrical features, *Astrophysical Journal*, under review
17. Nishimoto S, Watanabe K, Imada S et al. (2020b), Validation of EUV Emission Spectra During Solar Flares, *Earth, Planets and Space*, submitted to this issue
18. Otsuka Y, Ogawa T, Saito A, Tsugawa T, Fukao S, Miyazaki S (2002) A new technique for mapping of total electron content using GPS network in Japan. *Earth Planets Space* 54(1):63–70
19. Qian L, Burns. AG, Chamberlin. PC, Solomon SC (2011) Variability of thermosphere and ionosphere responses to solar flares. *Journal of Geophysical Research: Space Physics* 116:A10, A10309
20. Shinbori A, Otsuka Y, Sori T, Tsugawa T, Nishioka M (2020), Temporal and spatial variations of total electron content enhancements during a geomagnetic storm on 27 and 28 September 2017, *Journal of Geophysical Research: Space Physics*, 125, e2019JA026873
21. Solomon SC, Qian L (2005) Solar extreme-ultraviolet irradiance for general circulation models. *J Geophys Res* 110:A10306
22. Tsugawa T, Nishioka M, Ishii M, Hozumi K, Saito S, Shinbori A et al (2018) Total electron content observations by dense regional and worldwide international networks of GNSS. *Journal of Disaster Research* 13(3):535–545
23. Woods TN, Eparvier FG, Bailey SM et al (2005) Solar EUV Experiment (SEE): Mission overview and first results. *Journal of Geophysical Research: Space Physics* 110:A1, A01312

24. Woods TN, Hock R, Eparvier F et al (2011) New Solar Extreme-ultraviolet Irradiance Observations during Flares. *Astrophys J* 739:2, 59
25. Woods TN, Eparvier FG, Hock R et al (2012) Extreme Ultraviolet Variability Experiment (EVE) on the Solar Dynamics Observatory (SDO): Overview of Science Objectives, Instrument Design, Data Products, and Model Developments. *Sol Phys* 275:115–143

## Figures

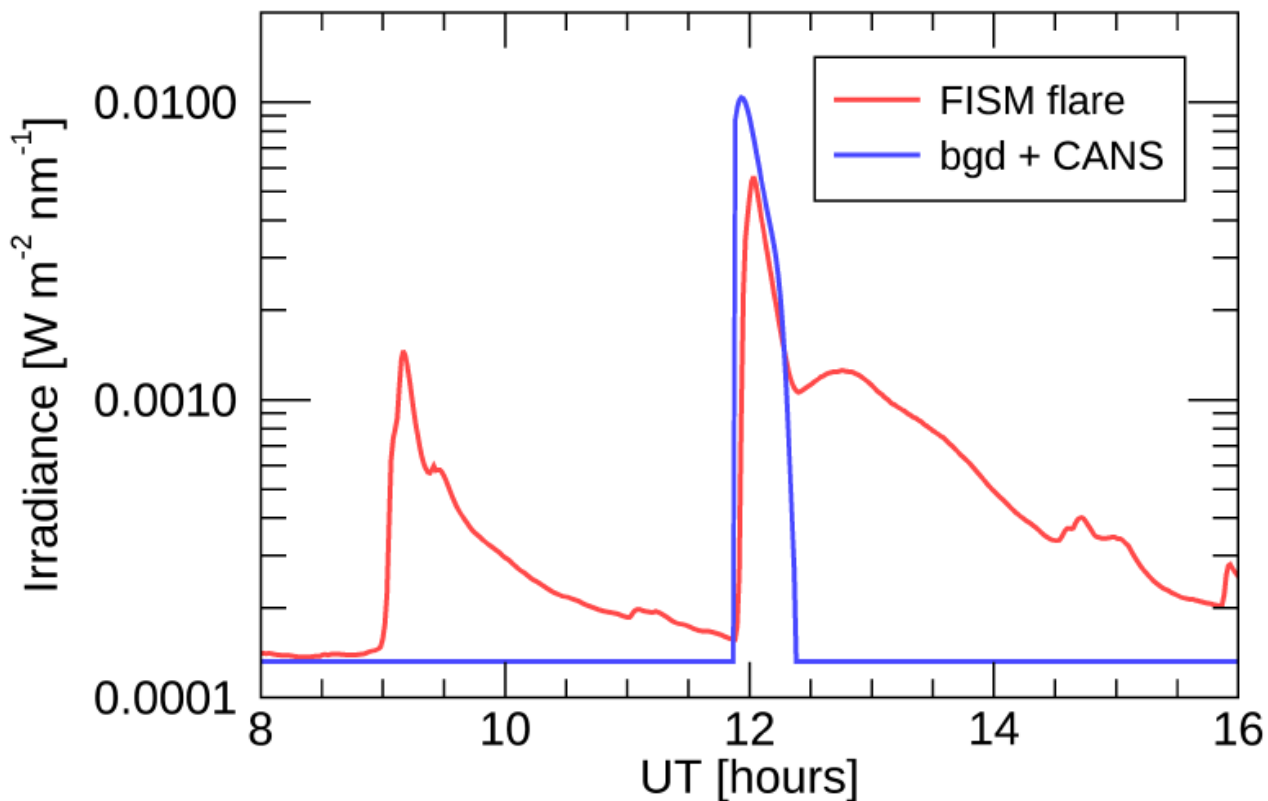


**Figure 1**

Light curve of soft X-ray (1-10 Å) emission “FISM flare” (red line) is proportional to the light curve of GOES soft X-ray (1-8 Å). “bgd” is the daily component of FISM and is a constant value. “CANS flare” reproduces only the light curve of the X9.3 flare during 11:53-12:24 UT. “bgd+CANS” (blue line) is the sum of the light curves of “bgd” and “CANS flare”.

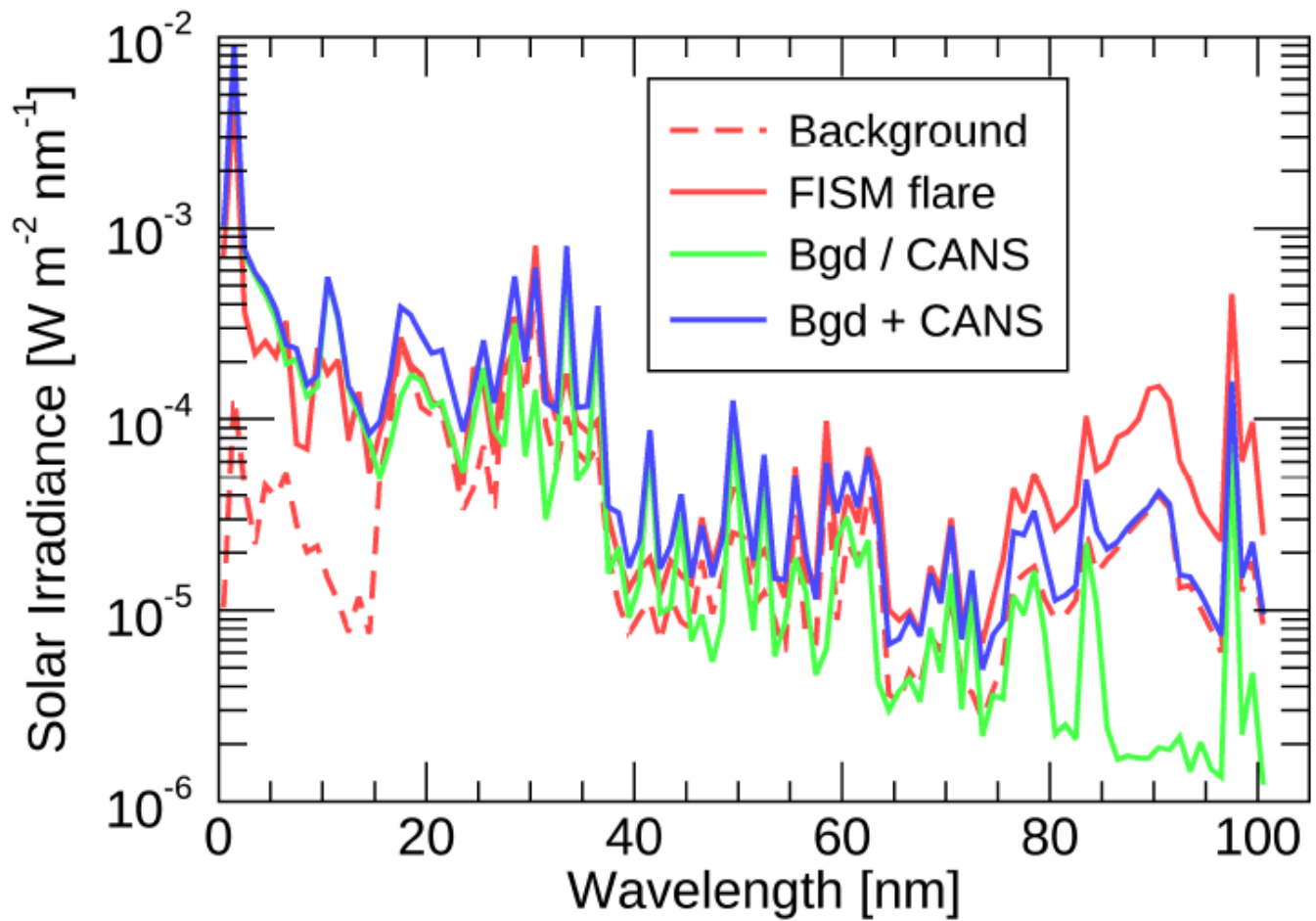
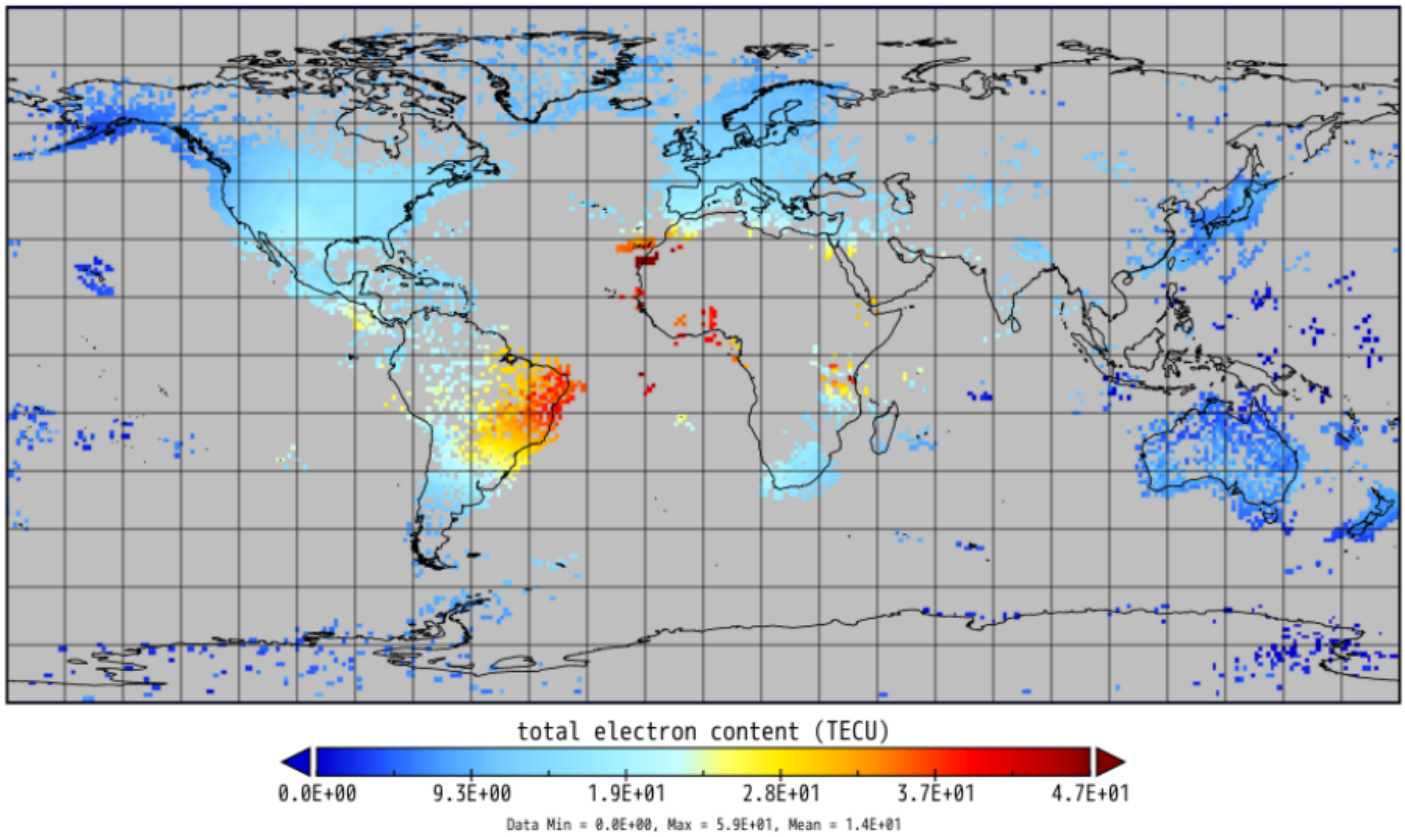


Figure 2

Emission spectra of X9.3 flare at 12 UT. The red solid line shows the FISM spectrum and the green solid line shows the CANS flare model spectrum. The blue solid line is the sum of the CANS flare model spectrum (green solid line) and the background (red dashed line). Since the CANS flare model does not consider the continuum component, there is no continuum component around 70-90 nm.

### total electron content



**Figure 3**

Distribution of TEC observed by global TEC (Drawing-TEC) at X9.3 class flare (12 UT) Distribution of TEC observed by global TEC (Drawing-TEC) at X9.3 class flare (12 UT). The European region was in the daytime at the time of the flare, and has sufficient data. Note: The designations employed and the presentation of the material on this map do not imply the expression of any opinion whatsoever on the part of Research Square concerning the legal status of any country, territory, city or area or of its authorities, or concerning the delimitation of its frontiers or boundaries. This map has been provided by the authors.

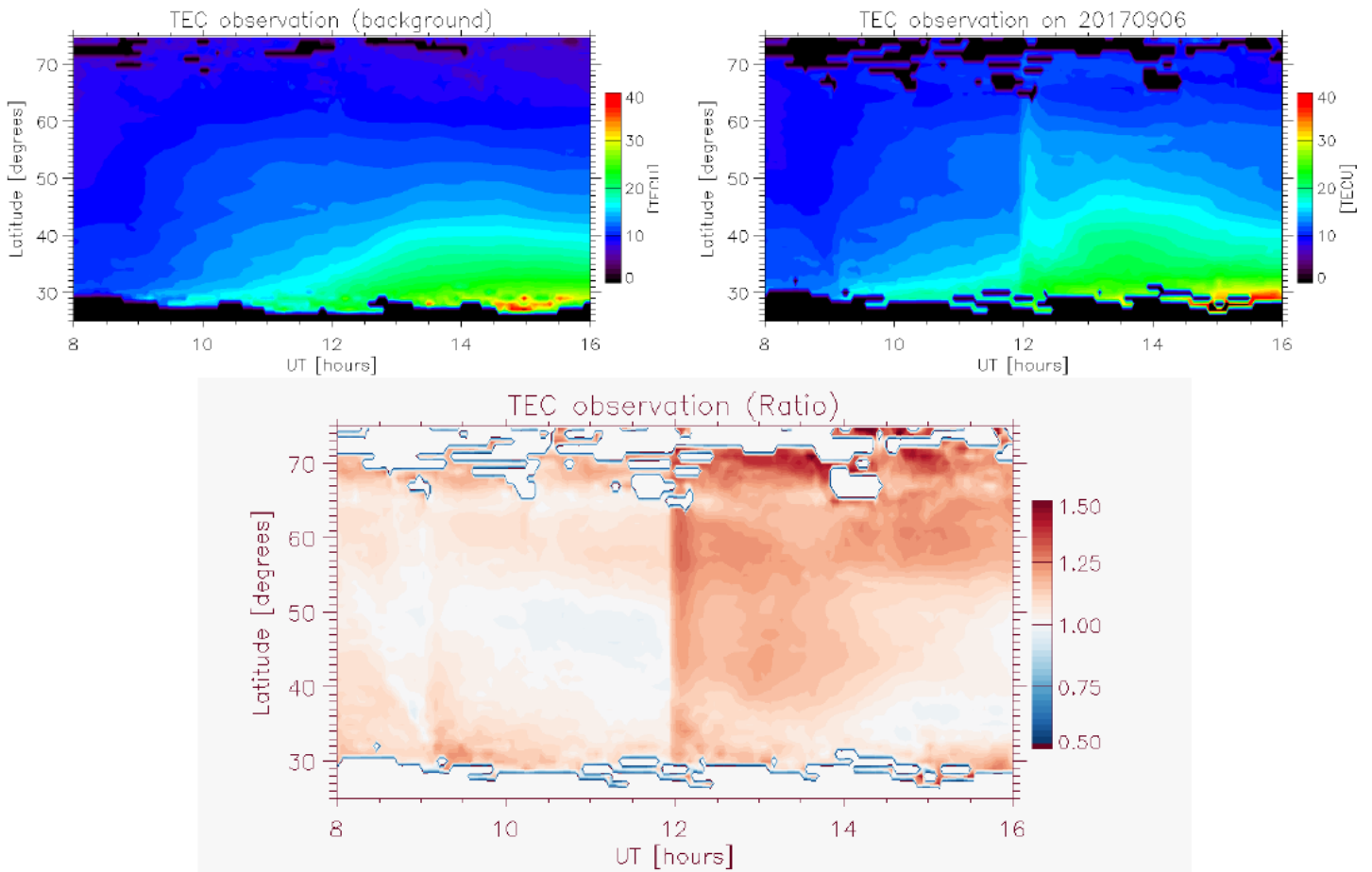


**Figure 4**

TEC observations at 0°E 25-75°N (Top left) Averaged TEC from September 1st to 10th, 2017. This is the background. (Top right) TEC on September 6, 2017. (Bottom) Ratio of TEC from flare (top right figure) and the background (top left figure). TEC significantly increases at any latitude when flare occurs.

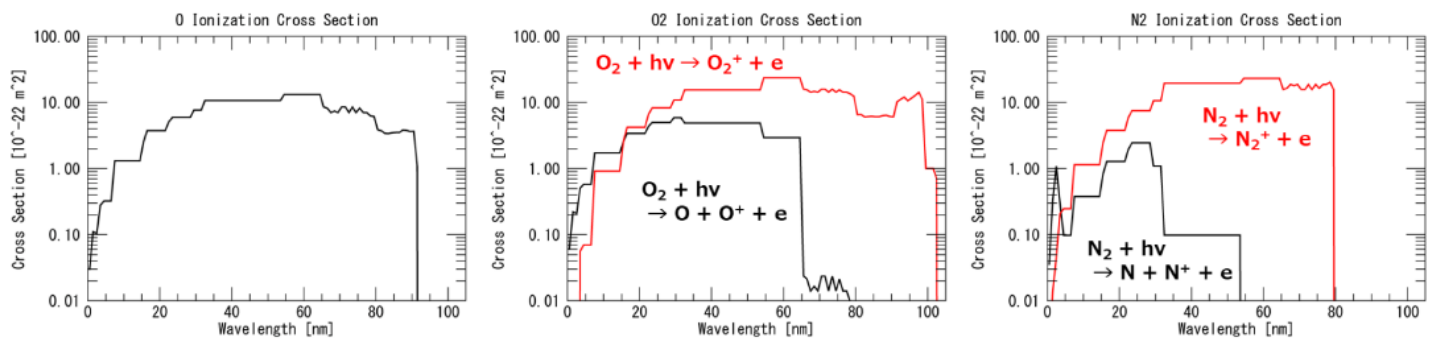


**Figure 5**

Photoionization and photo-dissociative ionization cross sections of major solar atmosphere atoms and molecules Photoionization and photo-dissociative ionization cross sections for each wavelength. (Left) Photoionization cross section of oxygen atom, (middle) cross section of photoionization and photo-

dissociative ionization of oxygen molecule, and (right) photoionization and photodissociation of nitrogen molecule. Cross section data is based on Solomon and Qian (2005).

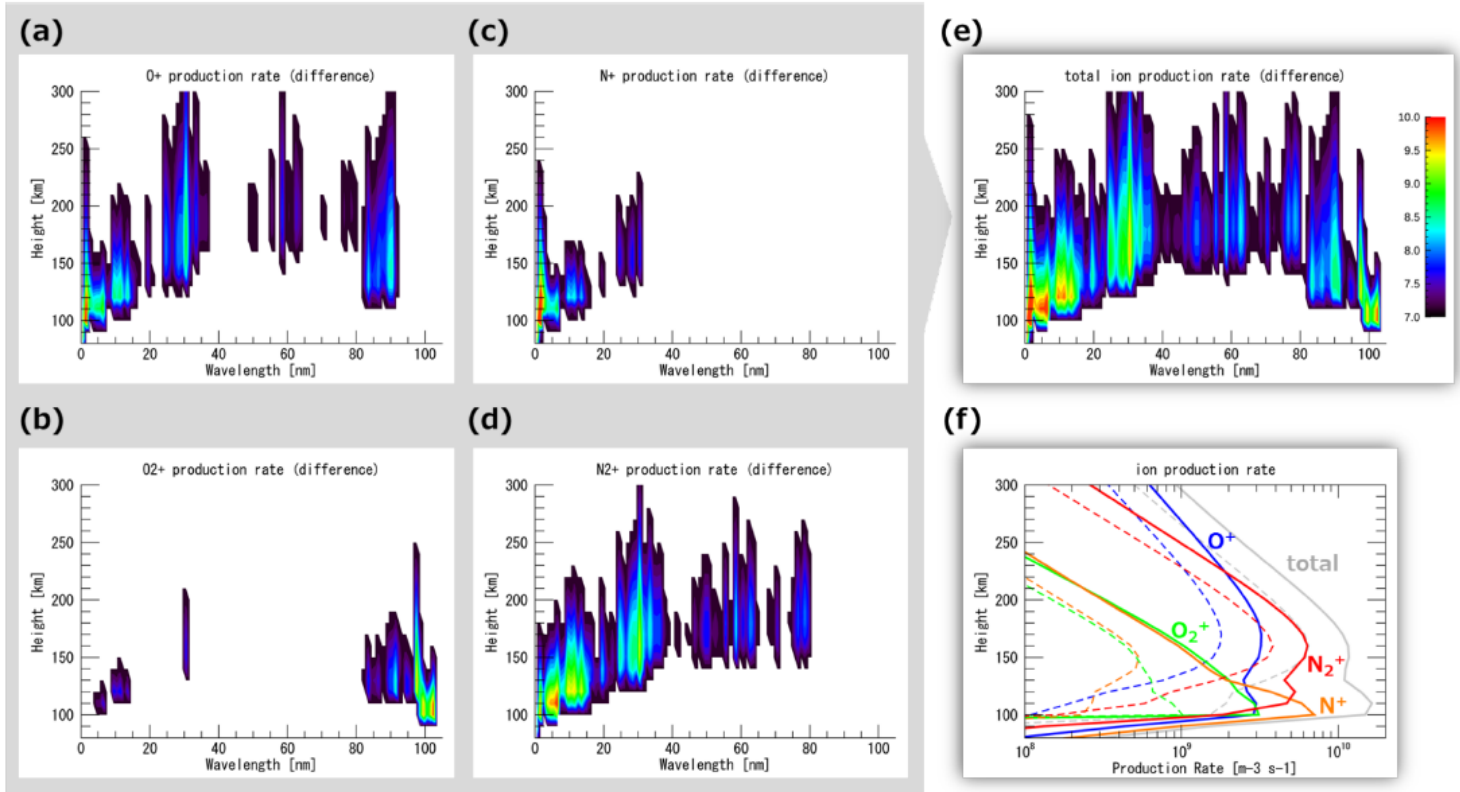


**Figure 6**

Difference of ionization rate due to X9.3 flare that occurred in September 2017. Difference in ionization rate of each ion at 0°E 30°N due to X9.3 flare that occurred in September 2017 including ionization by solar irradiance and ionization by secondary photoelectrons. FISM flare spectrum is used for the input spectrum to GAIA. Differences in ionization rate before and after flare for (a) O<sup>+</sup>, (b) O<sub>2</sub><sup>+</sup>, (c) N<sup>+</sup>, (d) N<sub>2</sub><sup>+</sup>, and (e) total ion as a function of the wavelength of solar irradiance (unit: Log<sub>10</sub>(W m<sup>-2</sup> nm<sup>-1</sup>)). (f) Differences in the altitude distribution of the ionization rate of each ion. Each solid line is just after the flare (12:00 UT), and each dotted line is before the flare (11:30 UT).

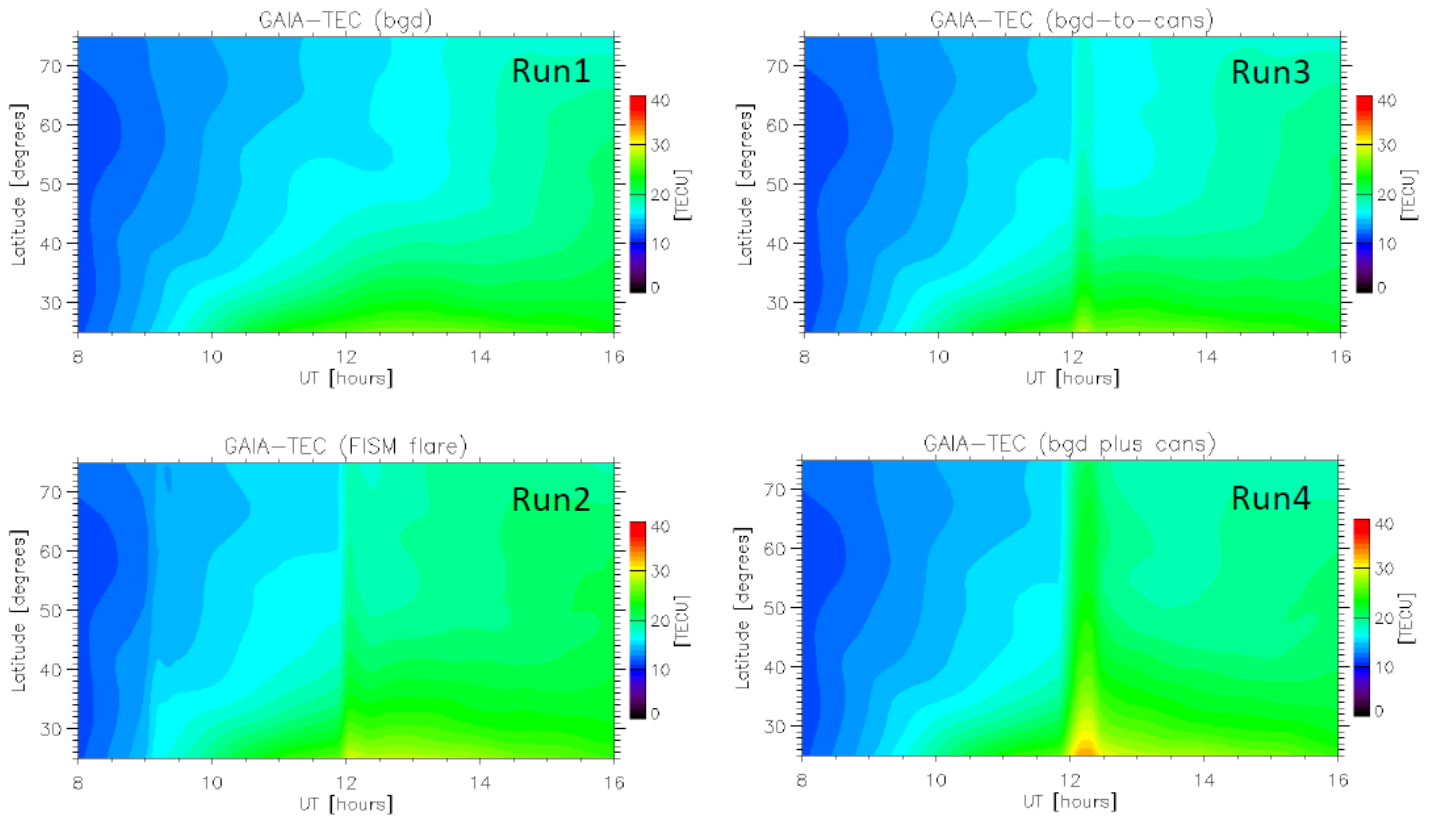


**Figure 7**

TEC distribution calculated by GAIA TEC distribution derived by inputting (upper left: Run1) background, (lower left: Run2) "FISM", (upper right: Run3) "CANS/bgD", and (lower right: Run4) "CANS+bgD" spectral changes.

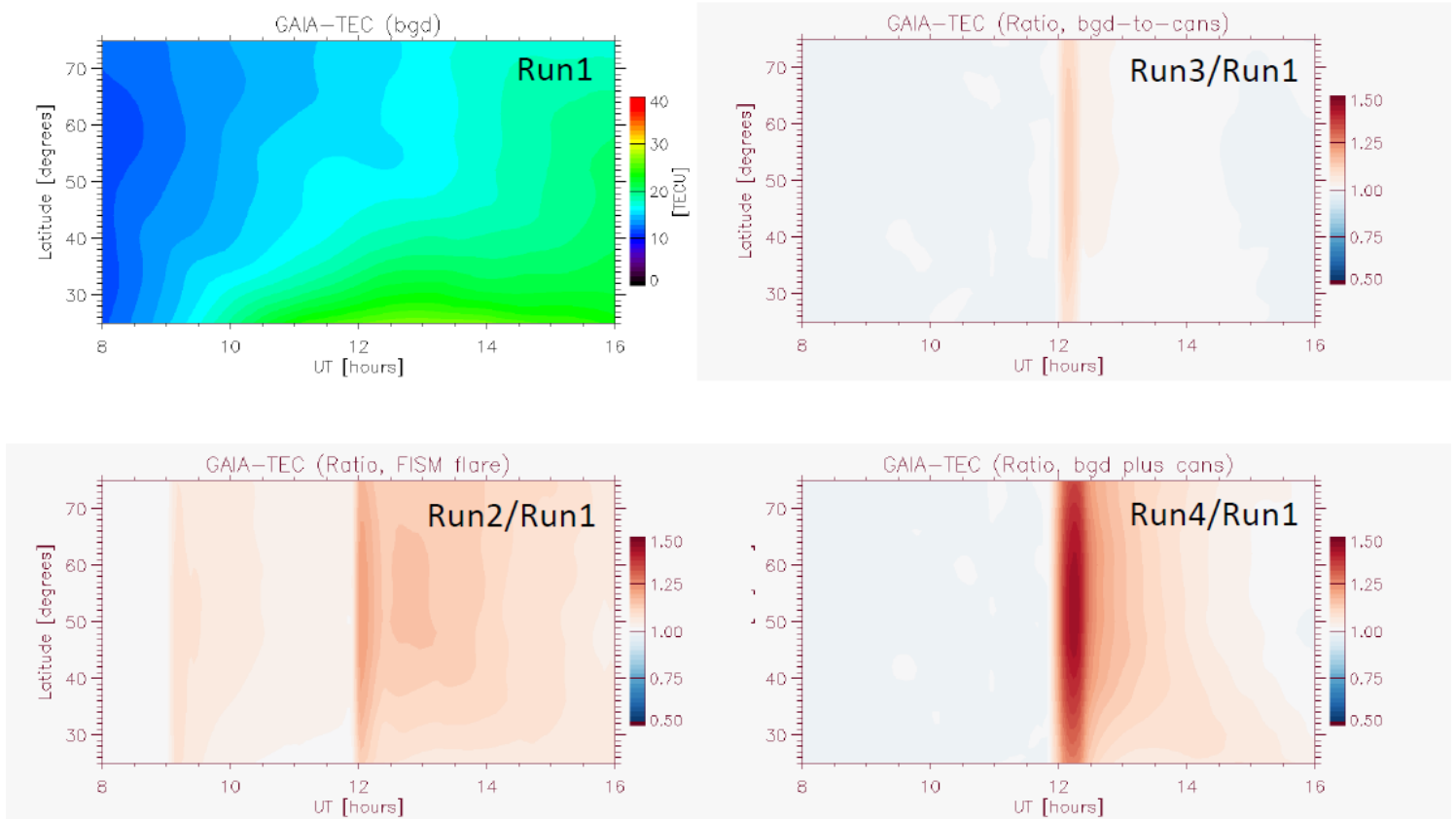


**Figure 8**

Ratio of TEC calculated by GAIA and the background Upper left: Background TEC distribution. Same as the top left figure in Figure 7. Lower left: Ratio of TEC for the “FISM” input (Run2/Run1). Upper right: Ratio of TEC for the “CANS/bgd” input (Run3/Run1). Lower right: Ratio of TEC for the “CANS+bgd” input (Run4/Run1).

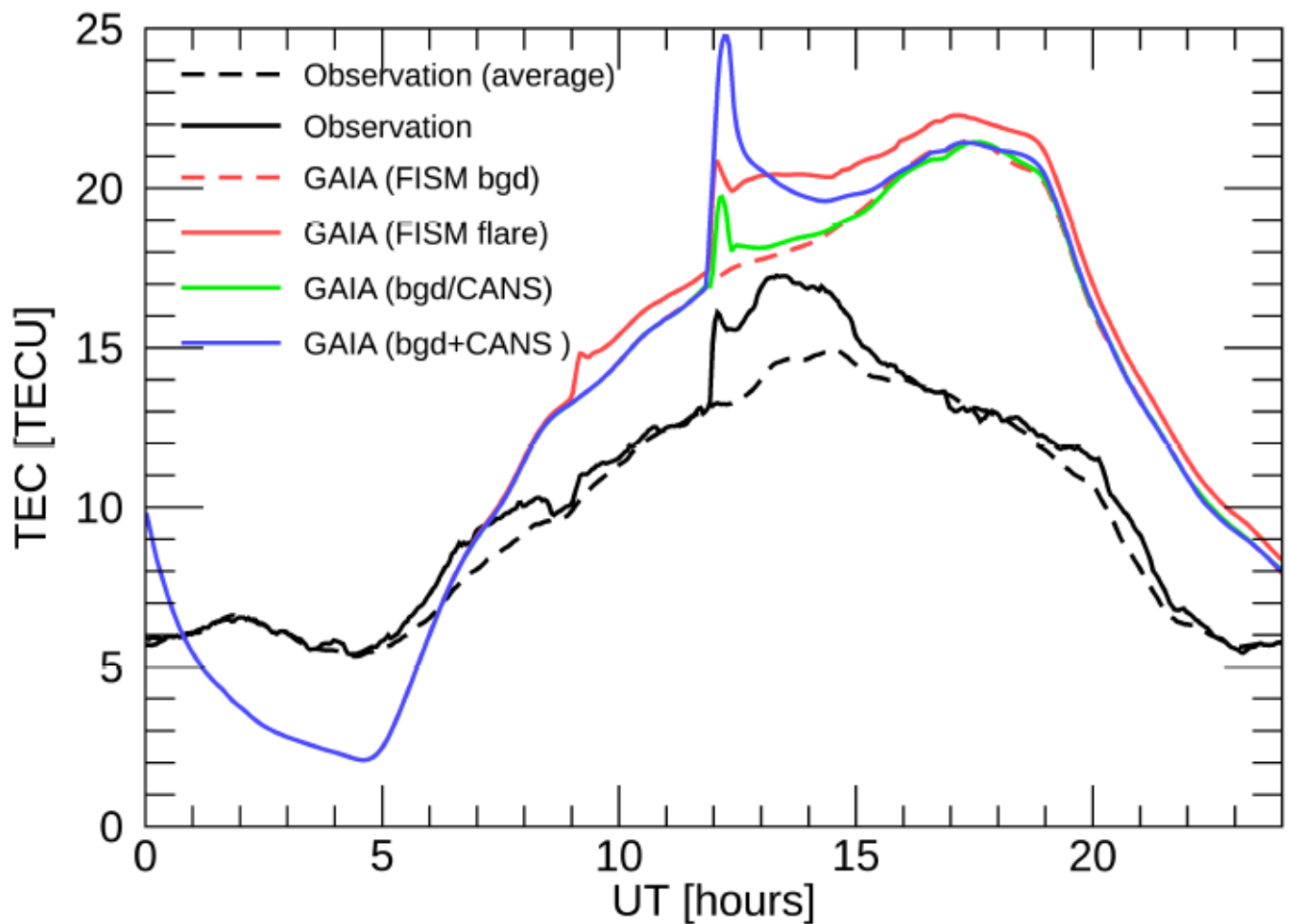


**Figure 9**

Variation of TEC at 0°E 44°N The solid black line is the observed value (top-right panel in Figure 4), and the dashed black line is the background of the observation (top-left panel in Figure 4). Red dashed line, red solid line, green line, and blue line are calculation results of GAIA with background input (Figure 7: Run1), "FISM" input (Figure 7: Run2), "CANS/bgd" input (Figure 7: Run3), and "CANS+bgd" input (Figure 7: Run4), respectively.

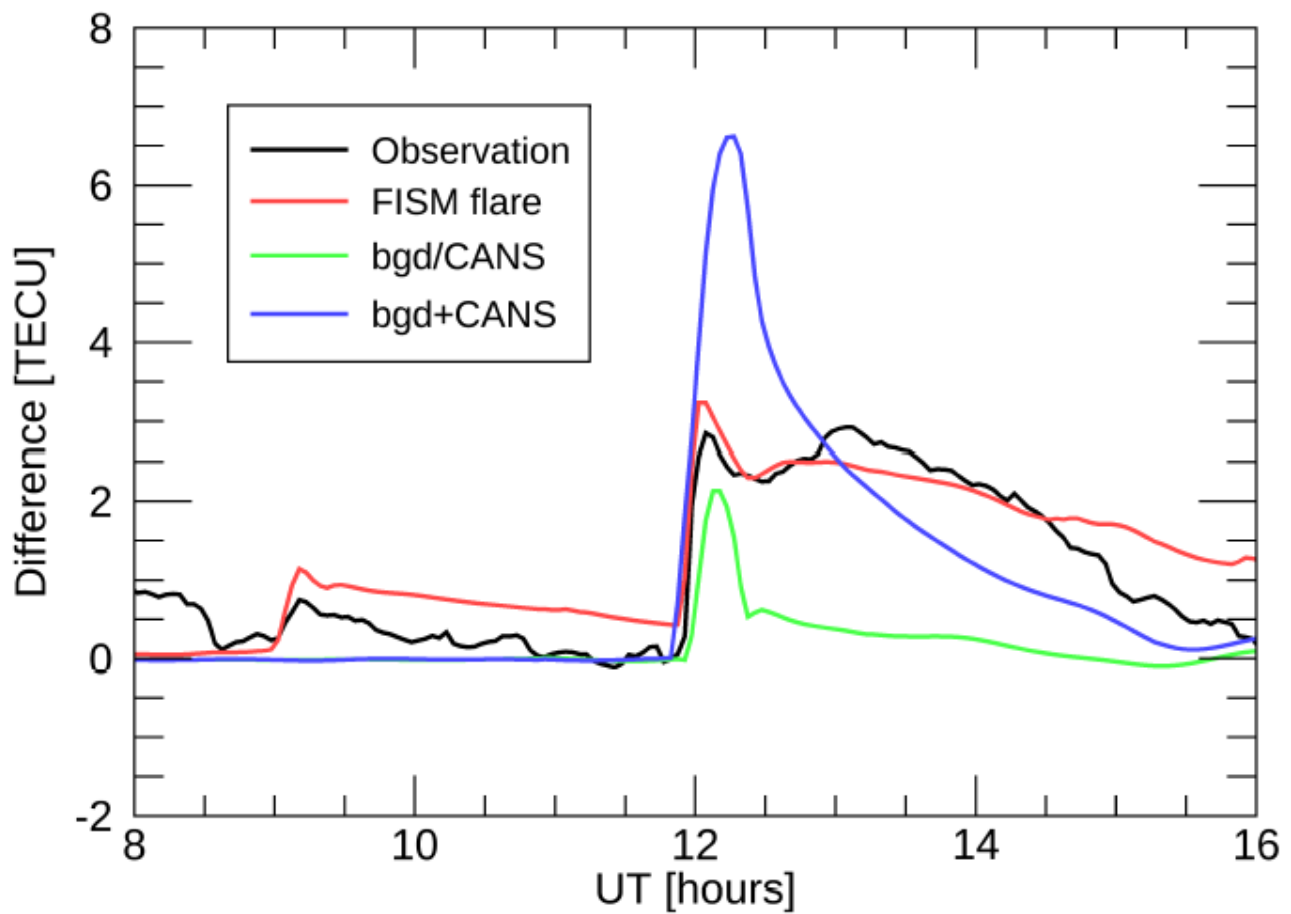


**Figure 10**

Difference of TEC from background at 0°E 44°N The black line is the difference of observed TEC to background. Red, green, and blue lines are the difference of calculation results of GAIA with “FISM” input, “CANS/bgd” input, and “CANS+bgd” input from background, respectively.

## Supplementary Files

This is a list of supplementary files associated with this preprint. Click to download.

- [FlareSpectraGAIAabst.pdf](#)